

Pattern dynamics in an annular CO₂ laser

M.L. Ramón¹, R. Meucci^{2,a}, E. Allaria², and S. Boccaletti¹¹ Dept. of Phys. and Applied Math., Universidad de Navarra, Irunlarrea s/n, 31080 Pamplona, Spain² Istituto Nazionale di Ottica Applicata, Largo E. Fermi 6, 50125 Firenze, Italy

Received 10 March 2000

Abstract. Competition among modes in an annular CO₂ laser has been experimentally and numerically analyzed. During the coexistence of different patterns, each of them resulting from the interaction of two transverse modes with opposite angular momentum, chaos has been experimentally detected. A numerical model, derived from the Maxwell-Bloch equations and including symmetry breaking terms, enables the interpretation of the main experimental features.

PACS. 42.55.-f Lasers – 42.65.Sf Dynamics of nonlinear optical systems; optical instabilities, optical chaos and complexity, and optical spatio-temporal dynamics – 42.65.-k Nonlinear optics

1 Introduction

Wide aperture lasers provide good experimental systems to investigate pattern formation and spatio-temporal dynamics. In this type of systems, the laser action occurs simultaneously for a considerable number of transverse modes, characterized by large values of the radial and azimuthal indices [1]. Their coexistence leads in most cases to patterns showing spatio-temporal behavior difficult to be analyzed [2–4].

From a theoretical point of view, symmetry arguments can simplify the approach to the problem of formation and dynamics of patterns. The equations describing a physical system (*e.g.* the Maxwell-Bloch equations in lasers, or the Navier-Stokes equation in fluids) can be reduced to model equations, such as the complex Swift-Hohenberg [5], Ginzburg-Landau [6] or Kuramoto-Sivashinsky ones [7]. The application of the bifurcation theory to these model equations leads to qualitative solutions helping in the interpretation of the experimental results [8–10]. In this context, the role of symmetries has been proved to be essential in the understanding of the phenomena. However, not only the global symmetry, but also the small asymmetries of the real systems have to be taken into account to reproduce the experimentally observed dynamics, as it can be seen for laser systems in [4, 10–12].

Previous works performed using CO₂ lasers emitting annularly symmetric intensity distributions [4, 12], have studied the role of infinitesimal symmetry imperfections of the system on the observed spatio-temporal dynamics. On the one hand, Huyet *et al.* [4] gave evidence of their influence on the dynamics of structures with high azimuthal index. On the other hand, Labate *et al.* [12]

analyzed the case of patterns with small azimuthal index near threshold, whose temporal behavior was theoretically explained as a Takens-Bogdanov bifurcation. In these two references, transitions are reported between different patterns, as well as temporal oscillations of the intensity in some spatial structures: periodic oscillations in [4], and aperiodic fluctuations determined by noise in [12].

Our study has been centered on a wide aperture CO₂ laser with annular symmetry, obtained by using a toroidal mirror as one of the cavity mirrors. This annular configuration with toroidal mirror provides a stable resonator that enables laser action only for those families of patterns preserving this symmetry, among all the modes present in a wide aperture laser.

Acting on the cavity detuning while operating the laser near the threshold region, we have experimentally studied the competition among few transverse modes of the optical cavity. This competition has been shown to lead to oscillatory or chaotic behavior. Experimental evidence of oscillatory or chaotic alternation of different transverse modes in an active optical system with large aperture had been already offered with respect to a photorefractive oscillator [13]. However, ours is the first controllable pattern alternation shown in a CO₂ laser. In order to compare with numerical results, we have developed (departing from the Maxwell-Bloch equations and taking into account breaking symmetry terms) the simplest model allowing the interpretation of nonlinear interactions between two different annular patterns. The derivation of the model includes new coupling terms accounting for the interaction of patterns with different angular momenta. The integration of the resulting equations reproduces qualitatively most of the experimentally observed dynamics.

The paper is organized as follows: in Section 2, the experimental setup and results are shown. Section 3 includes

^a e-mail: ric@ino.it

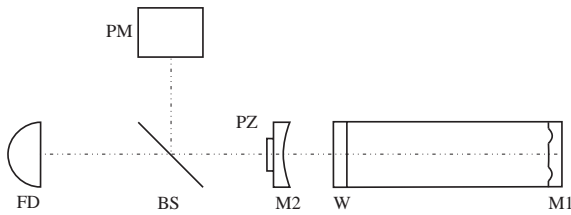


Fig. 1. Outline of the experimental setup. From right to left: M1 = toroidal mirror, W = window transparent to the infrared laser emission, M2 = outcoupler, PZ = piezoelectric translator, PM = powermeter, BS = beam splitter, and FD = fast detector.

numerical results, together with the derivation of the equations used in the numerical integration. Finally, Section 4 provides a general review on the results presented, and the conclusions.

2 Experimental setup and results

The experimental setup consists in a CO₂ laser with a Fabry-Perot configuration. An outline of the experimental device is sketched in Figure 1.

The 87-cm Fabry-Perot cavity consists of a spherical ZnSe outcoupler (38 mm diameter, 3000 mm radius of curvature, 90% reflection), and an annular copper mirror (1150 mm radius of curvature, 90% reflection) configured by the internal part of a torus, whose internal and external radii are 8 mm and 26 mm, respectively. The cavity length (the distance between these two mirrors) can be slightly modified by acting on a piezoelectric translator sustaining the outcoupler.

The active medium (4.5% CO₂, 82% He, 13.5% N₂) is pumped by means of a high-voltage DC discharge. This discharge is produced in a cylindrical Pyrex tube (500 mm length, 35.4 mm internal diameter) by means of two electrodes that preserve the annular symmetry of the system. All the experiences have been realized for discharge current values between 17 and 18 mA, at an average pressure of 23 mbar (in these conditions, the threshold current is between 15 and 16 mA).

By means of a Hg_xCd_{1-x}Te fast detector, we monitor the temporal evolution of the laser intensity in a given point of the pattern. The average output power is measured by means of a powermeter, and a CCD camera collects the image of the laser mode formed on a thermal image plate.

In this paper, we will focus on the interaction between two or more laser modes, that can be single-ring and also double-ring patterns. In a previous work performed with the same experimental configuration [14], we reported on the single-ring structures, whose number of lobes is always even, ranging from 22 to 36. In the present work, by means of a careful adjustment of the laser parameters, we also obtain laser action on double-ring patterns. These patterns set in only when the optical cavity is perfectly aligned (a small tilt of the order of 10⁻⁴ radians is sufficient to

prevent their appearance) and the laser gain (which depends on the discharge current and cooling temperature of the circulating water) is optimized with respect to the gas mixture average pressure. These structures can be observed either in a continuous and in a discrete form consisting of 34 lobes in both the external and internal rings (both of them with the same azimuthal index).

All these patterns, except in regimes of competition between them, show two different dynamical regimes: namely, an oscillating regime (with frequency ranging from 20 to 200 kHz), and a stable non oscillating regime. In some rare cases, they can also display a low-frequency irregular regime (frequency \approx 70 Hz).

In our experimental study, the cavity length has been used as a control parameter, enabling the transitions between different structures. Indeed, variations of the cavity length result into variations of the cavity detuning, and the resonance conditions for the different modes can be sequentially obtained. It is also possible to select a regime where two structures coexist, giving rise to diverse dynamical behaviors: alternancy between a regular oscillation and a non-oscillating regime, a single-frequency oscillation displaying an amplitude modulation, the alternancy between two oscillating regimes with different frequencies, and also windows of irregular temporal behavior. The passage from regular to irregular oscillating regimes can be visualized by means of a Poincaré section, performed by plotting the intensity minima of the temporal evolution in a given point of the pattern.

Figure 2 shows a situation where competition between more than two single-ring patterns arises. In Figure 2a, a period-1 regime can be seen around $t = 0.025$ s, *sandwiched* between irregular regimes wherein subharmonics of the fundamental frequency (\approx 21 kHz) appear. Looking at the power spectrum in these irregular regimes (Fig. 2b), the presence of the fundamental frequency and its subharmonics can be clearly noticed. In Figures 2c and 2d, we report two examples of irregular temporal oscillations. The transition from a period-one to an irregular oscillation can be distinctly appreciated in Figure 2c.

The competition between a single- and a double-ring pattern can be studied by changing the detuning starting from the optimal alignment conditions for the two-ring pattern. This double-ring structure has been usually found departing from a single annulus of 30 or 32 lobes. An increase of the cavity detuning yields the two-ring pattern, and eventually the subsequent appearance of the most stable single annulus of 24 lobes, usually related to higher power values. The detuning variations involved in this process are of the order of 50 MHz (the free spectral range of the cavity is 170 MHz). In Figures 3a and 3b we show the 24-lobe and the double-ring patterns, respectively. During the transitions between them, there is a major radial variation in the pattern shape (there is a change in the number of annulus of the structure, *i.e.*, in the radial index). The observation of irregular temporal behavior in this case confirms that this feature is related to the competition regime between different laser modes, independently of their radial indices. In Figure 4, we report

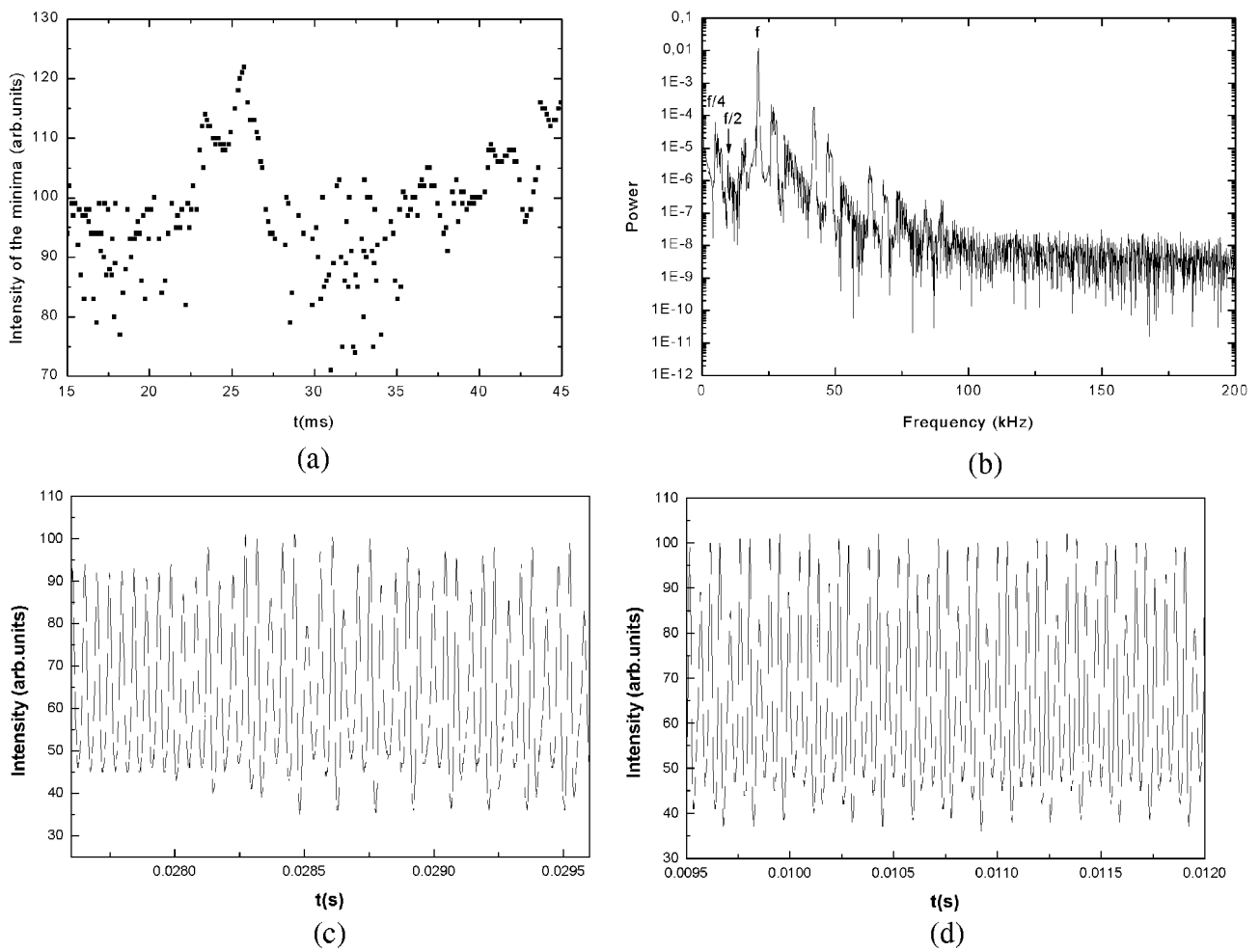


Fig. 2. Chaotic behavior in the interaction between more than two single-ring patterns. (a) Minima of the intensity oscillations. It can be noticed the presence of irregular regimes. (b) Power spectrum showing the fundamental frequency ($f \approx 21$ kHz) together with different subharmonics. (c) Transitions from a period-1 to an irregular regime. (d) Chaotic oscillations.

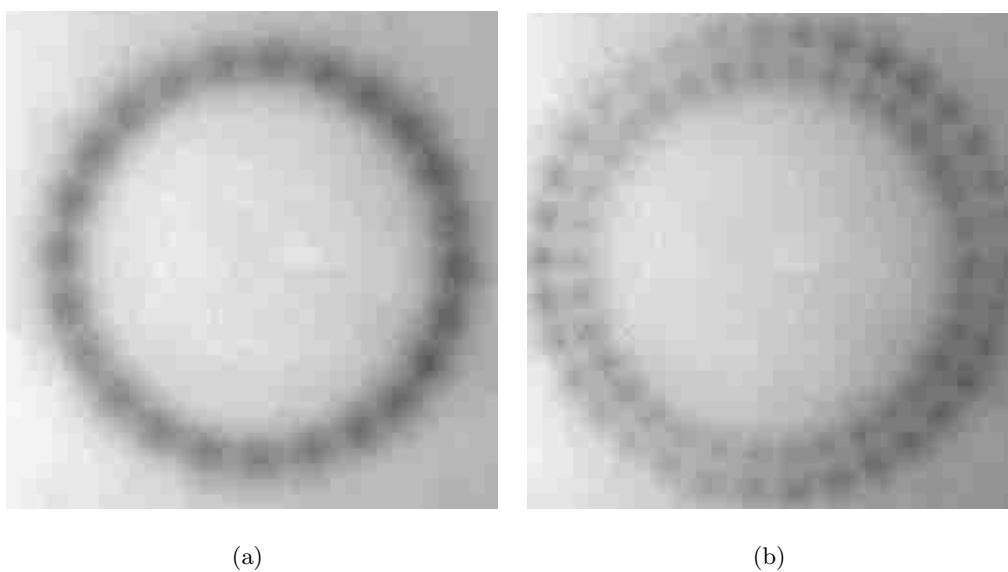


Fig. 3. (a) 24-lobe pattern with a slight continuous contribution. (b) Image of the double-ring pattern with 34 lobes in both annulus (the diameters of the internal and external rings are respectively 20 mm and 23.5 mm).

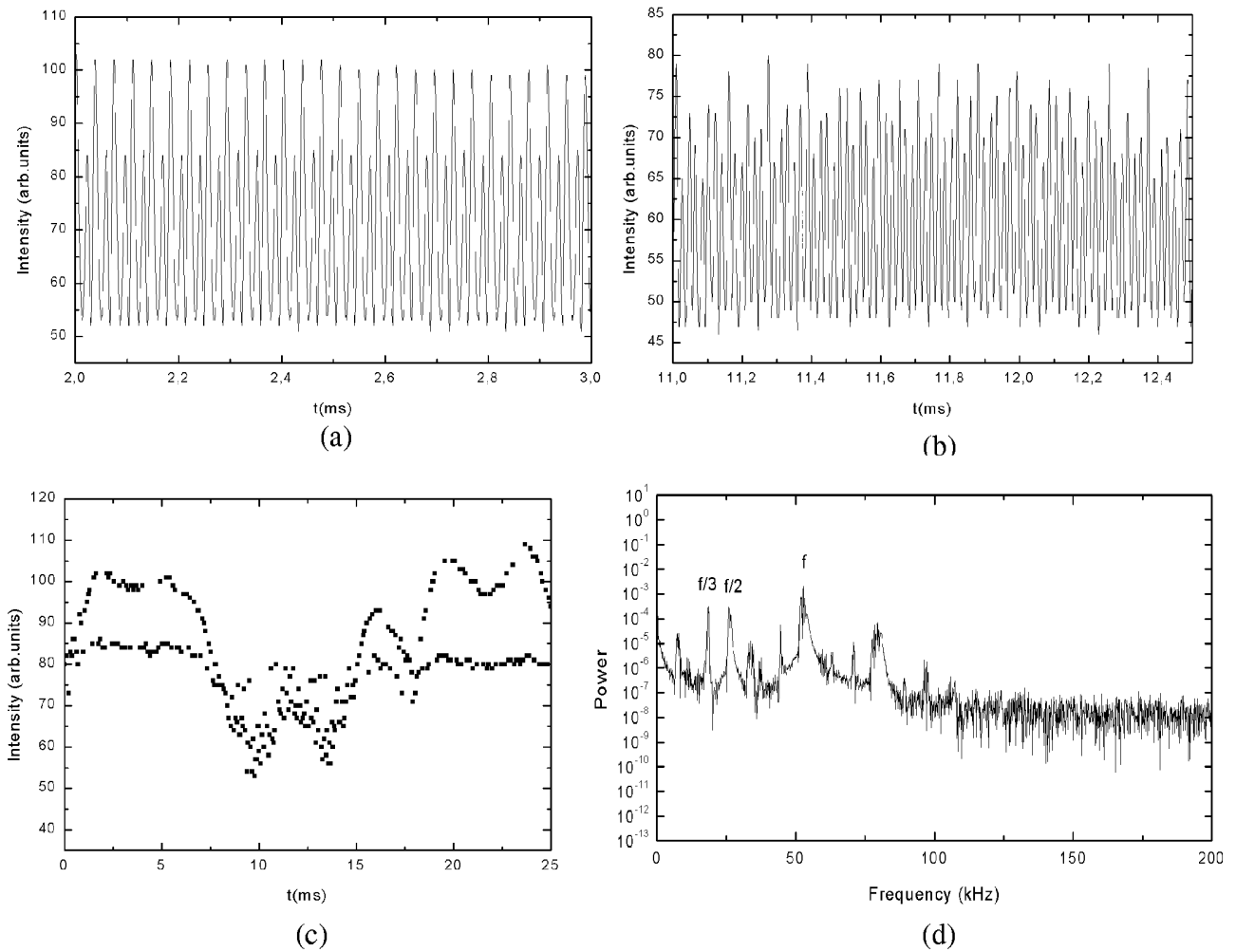


Fig. 4. Transition to chaos during the coexistence of the single- and double-ring structures. (a) Period-doubling regime. (b) Temporal representation of the intensity in a chaotic regime. (c) Stroboscopic record of the intensity, showing transitions between period-doubling and a chaotic regime. (d) Power spectrum showing the fundamental frequency ($f \approx 53$ kHz) together with the subharmonics $f/2$ and $f/3$, as well as different combinations of them.

the temporal behavior occurring during the transition between the double-ring pattern and the 24-lobe single-ring pattern. A clear period-doubling regime of the fundamental frequency f (about 53 kHz) is present in Figure 4a, whereas Figure 4b gives an example of the strongly irregular behavior following that regime. A stroboscopic record of the local intensity minima (Fig. 4c) shows clearly the alternancy between these two regimes. The corresponding power spectrum (Fig. 4d) contains not only the $f/2$ component, but also the $f/3$ contribution and combinations of them.

Finally, Figure 5a reports a non-uniform pattern, consisting of a double ring with three reinforced regions. This pattern displays highly irregular oscillations. In Figure 5b we report the power spectrum of the laser intensity, showing the fundamental frequency ($f \approx 38.8$ kHz), its subharmonic $f/5$ and different combinations of them. Figure 5c shows an alternation between regular and irregular oscillations.

3 Numerical analysis

The main dynamical features of the experimentally observed patterns can be captured by a simple model which can be derived from the Maxwell-Bloch equations:

$$\begin{aligned}
 \partial_t E - i\alpha \nabla^2 E &= -kE + gP \\
 \partial_t P &= -\gamma_{\perp} P + gEN \\
 \partial_t N &= -\gamma_{\parallel} (N - N_0) - \frac{g}{2} (E^* P + P^* E)
 \end{aligned} \tag{1}$$

where ∂_t stands for the partial derivative in time, $\nabla^2 \equiv \partial_x^2 + \partial_y^2$ is the Laplacian operator in the plane (x, y) transverse to the direction of light propagation in the cavity; E is the complex electromagnetic field, P is the complex polarization, N is the real population inversion, and N_0 is the value of the population inversion imposed by the pump mechanism; g is the coupling coefficient, $\alpha = c^2/2\omega$ (where c is the light speed in the vacuum, and ω is the main frequency for the longitudinal resonance); k , γ_{\perp} and

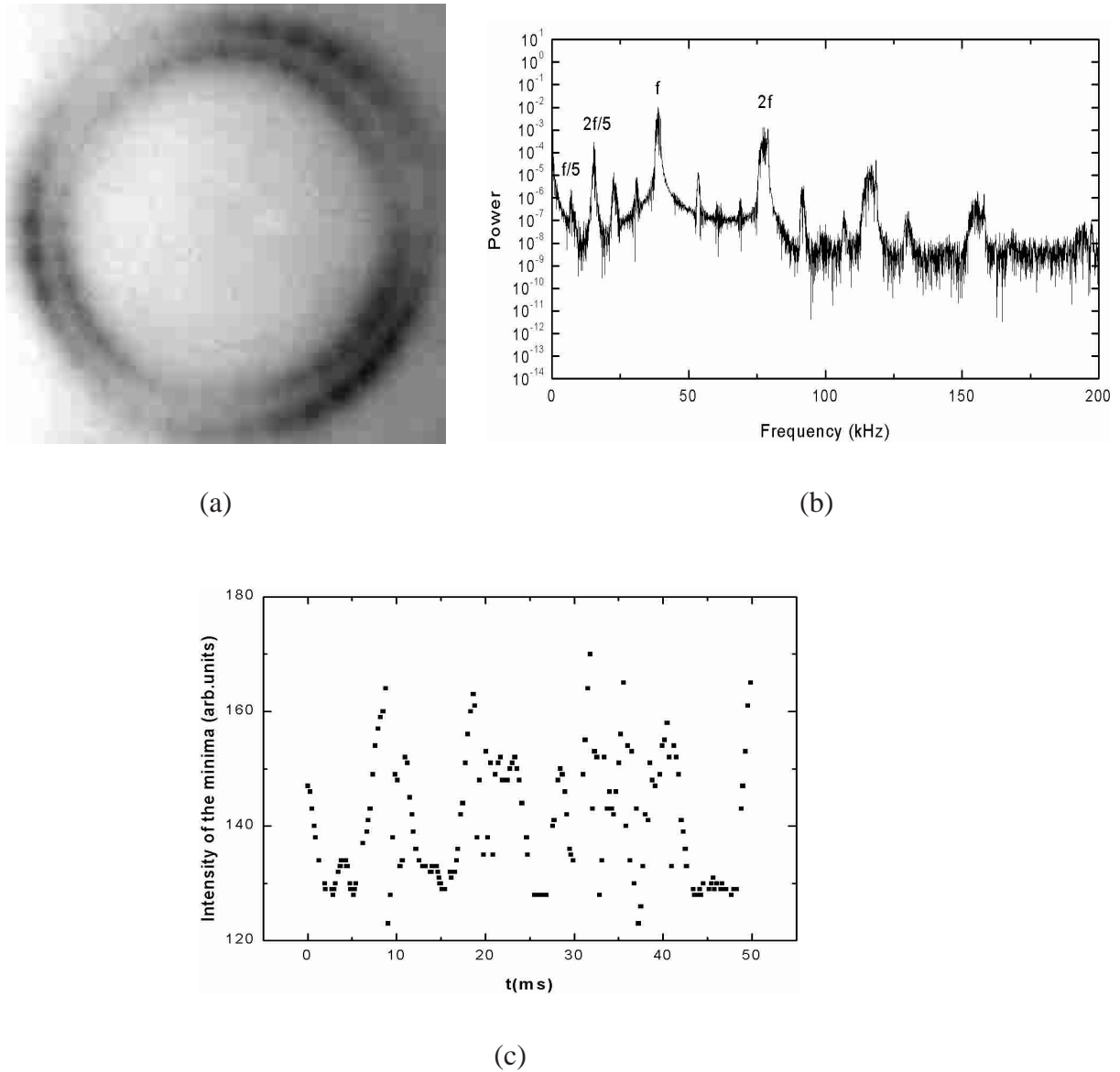


Fig. 5. Temporal evolution in a non-uniform double-ring pattern: (a) image of the non-uniform double-annulus structure; (b) power spectrum; (c) temporal evolution of the minima in an intensity-*versus*-time representation.

γ_{\parallel} are the decay rates for E , P and N , respectively. Equations (1) are obtained combining Maxwell equation for the field with Bloch equations for the active material, by filtering out a main longitudinal plane wave dependence (of frequency ω) in the electromagnetic field as well as in the polarization, and by considering the residual (secular) time and space variations of E and P .

In the following, we will make two further reductions. The first one consists in assuming our laser to behave as a class B laser, that is to verify $\gamma_{\perp} \gg \gamma_{\parallel}, k$. As a consequence, the second equation of (1) can be adiabatically eliminated ($\partial_t P \approx 0$) and the resulting expression for the polarization ($P = gEN/\gamma_{\perp}$) can be substituted into the first and the third of equations (1). The second reduction comes out by considering that all experimental results here reported correspond to pump values very close to the las-

ing threshold. In these conditions, one can safely assume that the dynamics of the laser reduces to a standard class A laser, that is $\partial_t N \approx 0$ [8]. Defining a saturation field $|E_{\text{sat}}|^2 = \gamma_{\perp}\gamma_{\parallel}/g^2$, and supposing to work with values of the field such that $|E|^2 \ll |E_{\text{sat}}|^2$, we obtain

$$N = \frac{1}{1 + \frac{|E|^2}{|E_{\text{sat}}|^2}} N_0. \quad (2)$$

Plugging (2) and the expression for P into (1), one obtains a single equation for E :

$$\partial_t E - i\alpha \nabla^2 E = -kE + \frac{g^2}{\gamma_{\perp}} \frac{N_0 E}{\left(1 + \frac{|E|^2}{|E_{\text{sat}}|^2}\right)} \quad (3)$$

that can be further simplified by defining $k_1 = -k + (g^2/\gamma_\perp)N_0$ and $k_2 = g^2N_0/(\gamma_\perp|E_{\text{sat}}|^2)$, and by approximating

$$\frac{1}{\left(1 + \frac{|E|^2}{|E_{\text{sat}}|^2}\right)} \simeq 1 - \frac{|E|^2}{|E_{\text{sat}}|^2}.$$

The final expression is:

$$\partial_t E - i\alpha \nabla^2 E = k_1 E - k_2 |E|^2 E. \quad (4)$$

Now, we have to make an assumption for the transverse dependence of the electromagnetic field. In the following, we will consider

$$E(r, t) = P_1(r)e^{i\omega t}(z_{11}(t)e^{im_1\theta} + z_{12}(t)e^{-im_1\theta}) + P_2(r)e^{i\omega t}(z_{21}(t)e^{im_2\theta} + z_{22}(t)e^{-im_2\theta}) \quad (5)$$

that is, we will consider the field as composed by the superposition of two annular patterns: two ring structures ($P_1(r)$ and $P_2(r)$) each one corresponding to a different angular momentum (m_1 and m_2). In equation (5), (r, θ) are the variables of the polar representation of the transverse plane, $P_1(r)$ and $P_2(r)$ are two different radial functions, and $z_{11}(t), z_{12}(t), z_{21}(t), z_{22}(t)$ are complex time dependent variables. In practice, each one-ring structure is seen as the combination of a rotating and a counterrotating wave, *i.e.*, two transverse modes with opposite angular momentum.

Introducing the expression (5) into the equation (4) and collecting the terms with the same angular resonance, the following set of complex equation is obtained:

$$\begin{aligned} \dot{z}_{11} &= A_1 z_{11} - B_1 z_{11}(|z_{11}|^2 + 2|z_{12}|^2) \\ &\quad - C_1 z_{11}(|z_{21}|^2 + |z_{22}|^2) - C_1 z_{22} z_{12}^* z_{21} \\ \dot{z}_{12} &= A_1 z_{12} - B_1 z_{12}(|z_{12}|^2 + 2|z_{11}|^2) \\ &\quad - C_1 z_{12}(|z_{21}|^2 + |z_{22}|^2) - C_1 z_{22} z_{11}^* z_{21} \\ \dot{z}_{21} &= A_2 z_{21} - B_2 z_{21}(|z_{21}|^2 + 2|z_{22}|^2) \\ &\quad - C_2 z_{21}(|z_{11}|^2 + |z_{12}|^2) - C_2 z_{12} z_{22}^* z_{11} \\ \dot{z}_{22} &= A_2 z_{22} - B_2 z_{22}(|z_{22}|^2 + 2|z_{21}|^2) \\ &\quad - C_2 z_{22}(|z_{11}|^2 + |z_{12}|^2) - C_2 z_{12} z_{21}^* z_{11} \end{aligned} \quad (6)$$

where dots denote temporal derivatives, and the parameters A, B and C are given by:

$$\begin{aligned} A_n &= -i\omega + i\frac{\alpha}{\alpha_n}(\beta_n + \gamma_n - \delta_n) + k_n, \\ B_n &= \frac{\mu_n}{\alpha_n}, \\ C_n &= 2\frac{\nu_n}{\alpha_n}, \end{aligned} \quad (7)$$

($n = 1, 2$). In equations (7), the values of $\alpha, \beta, \gamma, \delta, \mu$ and ν can be related to the fundamental parameters of

the Maxwell-Bloch equations as follows

$$\begin{aligned} \alpha_n &= \int_{-\infty}^{+\infty} P_n(r) dr, & \beta_n &= \int_{-\infty}^{+\infty} \frac{d^2 P_n(r)}{dr^2} dr, \\ \gamma_n &= \int_{-\infty}^{+\infty} \frac{1}{r} \frac{dP_n(r)}{dr} dr, & \delta_n &= m_n^2 \int_{-\infty}^{+\infty} \frac{P_n(r)}{r^2} dr, \\ \mu_n &= k_2 \int_{-\infty}^{+\infty} P_n^3(r) dr, & \nu_1 &= k_2 \int_{-\infty}^{+\infty} P_1(r) P_2^2(r) dr, \\ \nu_2 &= k_2 \int_{-\infty}^{+\infty} P_2(r) P_1^2(r) dr. \end{aligned} \quad (8)$$

An important outcome is that the parameters A are complex, whereas B and C are real. The last step consists in separating real and imaginary parts in the equations, by writing $z_{lj} = \rho_{lj} e^{i\varphi_{lj}}$ ($l, j = 1, 2$). The resulting equations are

$$\begin{aligned} \dot{\rho}_{11} &= \Re(A_1)\rho_{11} - B_1\rho_{11}(\rho_{11}^2 + 2\rho_{12}^2) - C_1\rho_{11}(\rho_{21}^2 + \rho_{22}^2) \\ &\quad - C_1\rho_{22}\rho_{12}\rho_{21} \cos \Delta, \\ \dot{\rho}_{12} &= \Re(A_1)\rho_{12} - B_1\rho_{12}(\rho_{12}^2 + 2\rho_{11}^2) - C_1\rho_{12}(\rho_{21}^2 + \rho_{22}^2) \\ &\quad - C_1\rho_{22}\rho_{11}\rho_{21} \cos \Delta, \\ \dot{\rho}_{21} &= \Re(A_2)\rho_{21} - B_2\rho_{21}(\rho_{21}^2 + 2\rho_{22}^2) - C_2\rho_{21}(\rho_{11}^2 + \rho_{12}^2) \\ &\quad - C_2\rho_{12}\rho_{22}\rho_{11} \cos \Delta, \\ \dot{\rho}_{22} &= \Re(A_2)\rho_{22} - B_2\rho_{22}(\rho_{22}^2 + 2\rho_{21}^2) - C_2\rho_{22}(\rho_{11}^2 + \rho_{12}^2) \\ &\quad - C_2\rho_{12}\rho_{21}\rho_{11} \cos \Delta, \\ \dot{\varphi}_{11} &= \Im(A_1) - C_1(\rho_{22}\rho_{12}\rho_{21}/\rho_{11}) \sin \Delta, \\ \dot{\varphi}_{12} &= \Im(A_1) - C_1(\rho_{22}\rho_{11}\rho_{21}/\rho_{12}) \sin \Delta, \\ \dot{\varphi}_{21} &= \Im(A_2) + C_2(\rho_{12}\rho_{22}\rho_{11}/\rho_{21}) \sin \Delta, \\ \dot{\varphi}_{22} &= \Im(A_2) + C_2(\rho_{12}\rho_{21}\rho_{11}/\rho_{22}) \sin \Delta, \end{aligned} \quad (9)$$

where $\Delta = \varphi_{21} + \varphi_{22} - \varphi_{11} - \varphi_{12}$.

Equations (9) describe the dynamics of the system close to threshold in a perfect cylindrical symmetry. In realistic experimental conditions, it is unavoidable the presence of small imperfections breaking such a symmetry. To account for symmetry breaking mechanisms, we heuristically introduce a new term to be added in the right hand side of equation (6), which now become

$$\begin{aligned} \dot{z}_{11} &= A_1 z_{11} - B_1 z_{11}(|z_{11}|^2 + 2|z_{12}|^2) \\ &\quad - C_1 z_{11}(|z_{21}|^2 + |z_{22}|^2) - C_1 z_{22} z_{12}^* z_{21} + \epsilon z_{12} \\ \dot{z}_{12} &= A_1 z_{12} - B_1 z_{12}(|z_{12}|^2 + 2|z_{11}|^2) \\ &\quad - C_1 z_{12}(|z_{21}|^2 + |z_{22}|^2) - C_1 z_{22} z_{11}^* z_{21} + \epsilon z_{11} \\ \dot{z}_{21} &= A_2 z_{21} - B_2 z_{21}(|z_{21}|^2 + 2|z_{22}|^2) \\ &\quad - C_2 z_{21}(|z_{11}|^2 + |z_{12}|^2) - C_2 z_{12} z_{22}^* z_{11} + \epsilon z_{22} \\ \dot{z}_{22} &= A_2 z_{22} - B_2 z_{22}(|z_{22}|^2 + 2|z_{21}|^2) \\ &\quad - C_2 z_{22}(|z_{11}|^2 + |z_{12}|^2) - C_2 z_{12} z_{21}^* z_{11} + \epsilon z_{21} \end{aligned} \quad (10)$$

$$\begin{aligned}
\dot{\rho}_{11} &= \Re(A_1)\rho_{11} - B_1\rho_{11}(\rho_{11}^2 + 2\rho_{12}^2) - C_1\rho_{11}(\rho_{21}^2 + \rho_{22}^2) - C_1\rho_{22}\rho_{12}\rho_{21} \cos \Delta + \rho_\epsilon\rho_{12} \cos(\varphi_\epsilon + \varphi_{12} - \varphi_{11}) \\
\dot{\rho}_{12} &= \Re(A_1)\rho_{12} - B_1\rho_{12}(\rho_{12}^2 + 2\rho_{11}^2) - C_1\rho_{12}(\rho_{21}^2 + \rho_{22}^2) - C_1\rho_{22}\rho_{11}\rho_{21} \cos \Delta + \rho_\epsilon\rho_{11} \cos(\varphi_\epsilon + \varphi_{11} - \varphi_{12}) \\
\dot{\rho}_{21} &= \Re(A_2)\rho_{21} - B_2\rho_{21}(\rho_{21}^2 + 2\rho_{22}^2) - C_2\rho_{21}(\rho_{11}^2 + \rho_{12}^2) - C_2\rho_{12}\rho_{22}\rho_{11} \cos \Delta + \rho_\epsilon\rho_{22} \cos(\varphi_\epsilon + \varphi_{22} - \varphi_{21}) \\
\dot{\rho}_{22} &= \Re(A_2)\rho_{22} - B_2\rho_{22}(\rho_{22}^2 + 2\rho_{21}^2) - C_2\rho_{22}(\rho_{11}^2 + \rho_{12}^2) - C_2\rho_{12}\rho_{21}\rho_{11} \cos \Delta + \rho_\epsilon\rho_{21} \cos(\varphi_\epsilon + \varphi_{21} - \varphi_{22}) \\
\dot{\varphi}_{11} &= \Im(A_1) - C_1(\rho_{22}\rho_{12}\rho_{21}/\rho_{11}) \sin \Delta + (\rho_\epsilon\rho_{12}/\rho_{11}) \sin(\varphi_\epsilon + \varphi_{12} - \varphi_{11}) \\
\dot{\varphi}_{12} &= \Im(A_1) - C_1(\rho_{22}\rho_{11}\rho_{21}/\rho_{12}) \sin \Delta + (\rho_\epsilon\rho_{11}/\rho_{12}) \sin(\varphi_\epsilon + \varphi_{11} - \varphi_{12}) \\
\dot{\varphi}_{21} &= \Im(A_2) + C_2(\rho_{12}\rho_{22}\rho_{11}/\rho_{21}) \sin \Delta + (\rho_\epsilon\rho_{22}/\rho_{21}) \sin(\varphi_\epsilon + \varphi_{22} - \varphi_{21}) \\
\dot{\varphi}_{22} &= \Im(A_2) + C_2(\rho_{12}\rho_{21}\rho_{11}/\rho_{22}) \sin \Delta + (\rho_\epsilon\rho_{21}/\rho_{22}) \sin(\varphi_\epsilon + \varphi_{21} - \varphi_{22})
\end{aligned} \tag{11}$$

where $\epsilon = \rho_\epsilon e^{i\varphi_\epsilon}$ is a complex parameter. It is important to remark that ϵ is the only parameter which cannot be extracted directly from first principles, since it depends on the particular laboratory conditions. The ϵ parameter corresponds to a breaking of the rotational symmetry, which, however, preserves the reflectional symmetry. A similar symmetry breaking term was considered in reference [12] for studying the symmetry breaking effects in the dynamics of a single-ring pattern.

Another important remark on the structure of equations (10) is that, while the terms multiplied by the parameters B_1 and B_2 represent the inter-mode coupling and they were already introduced in references [4, 10, 12], the new terms multiplied by the parameters C_1 and C_2 are the cross-mode contributions to the coupling. These terms (here directly extracted from the Maxwell-Bloch equations) are considered in order to describe the interaction between modes having different angular momenta.

The new equations are

see equations (11) above.

It is interesting to analyze the obtained equations. First of all, the parameters A can be interpreted as the effective gain of each mode, whereas the parameters B represent the interaction of the two components of the same radial mode (the propagating and counterpropagating wave at the same m). By comparing our results with the equations obtained by Labate *et al.* [12], one can easily realize that these last ones are the particular case of equations (11) when $C = 0$. The terms which are multiplied by C (directly derived from the Maxwell-Bloch equations) describe the interaction between different radial modes, and will be taken different than zero in all our numerics.

Furthermore, the expressions for B and C are complicated functions of the radial shape of the mode. Therefore, if the selected modes show similar radial shapes (as *e.g.* in the case of two modes with similar azimuthal index), the corresponding parameters will verify $B_1 \approx B_2$ and $C_1 \approx C_2$. As for ϵ , we have assumed the same values reported in reference [12] ($\rho_\epsilon = 0.5$, $\varphi_\epsilon = 1.059$), which conveniently describe a typical laboratory situation.

In the following, we have integrated equations (11) so as to reproduce numerically the main features of the experimental results. Our first step was to reproduce the

case of a double ring structure with three reinforced regions (see Fig. 5). To this purpose, we have selected the following Gauss-Laguerre functions in equation (5)

$$\begin{aligned}
P_1(r) &= \frac{2}{\sqrt{\pi}} (2r^2)^{m_1/2} \sqrt{\frac{p_1!}{(m_1 + p_1)!}} e^{-r^2}, \\
P_2(r) &= \frac{2}{\sqrt{\pi}} (-2r^2 + m_2 + 1) (2r^2)^{m_2/2} \sqrt{\frac{p_2!}{(m_2 + p_2)!}} e^{-r^2},
\end{aligned} \tag{12}$$

with $m_1 = 14$, $m_2 = 17$, $p_1 = 0$, $p_2 = 1$, where index 1 (2) corresponds to a 28-lobe single-ring (34-lobe double-ring) pattern. In equations (12), $m_{1,2}$ ($p_{1,2}$) are the azimuthal (radial) indices. The Gauss-Laguerre modes can be considered, indeed, a sensible basis onto which to project the laser equations [17] (see also the review paper [1]). In Figure 6 we report a simulation of system (11) with $A_1^i = A_2^i = 1.4489$, $A_1^r = 1$, $A_2^r = 4$, $B_1 = 1.05$, $B_2 = 0.15$, $C_1 = C_2 = 0.1$, $\rho_\epsilon = 0.5$, $\varphi_\epsilon = 1.059$. The two functions involved are represented in Figures 6a and 6b. The competition between these two patterns gives rise to a structure composed by two rings with three reinforced regions (Fig. 6c), associated with an irregular temporal evolution of the laser intensity (Fig. 6e), whose power spectrum (Fig. 6d) is dominated by two main frequencies with all nonlinear combinations.

The case of an emerging single ring structure can be also simulated in equations (11), by selecting

$$\begin{aligned}
P_1(r) &= \frac{2}{\sqrt{\pi}} (2r^2)^{m_1/2} \sqrt{\frac{p_1!}{(m_1 + p_1)!}} e^{-r^2}, \\
P_2(r) &= \frac{2}{\sqrt{\pi}} (2r^2)^{m_2/2} \sqrt{\frac{p_2!}{(m_2 + p_2)!}} e^{-r^2},
\end{aligned} \tag{13}$$

where $p_1 = p_2 = 0$, $m_1 = 12$, $m_2 = 14$ (two single-ring patterns with 24 and 28 lobes, respectively). The results are reported in Figure 7 for the following parameter choice: $A_1^i = A_2^i = 1.4489$, $A_1^r = 13$, $A_2^r = 12$, $B_1 = 0.5$, $B_2 = 1$, $C_1 = C_2 = 0.1$, $\rho_\epsilon = 0.5$, $\varphi_\epsilon = 1.059$. The resulting pattern is shown in Figure 7a. Figure 7b reports the power spectrum of the irregular temporal evolution of the laser intensity.

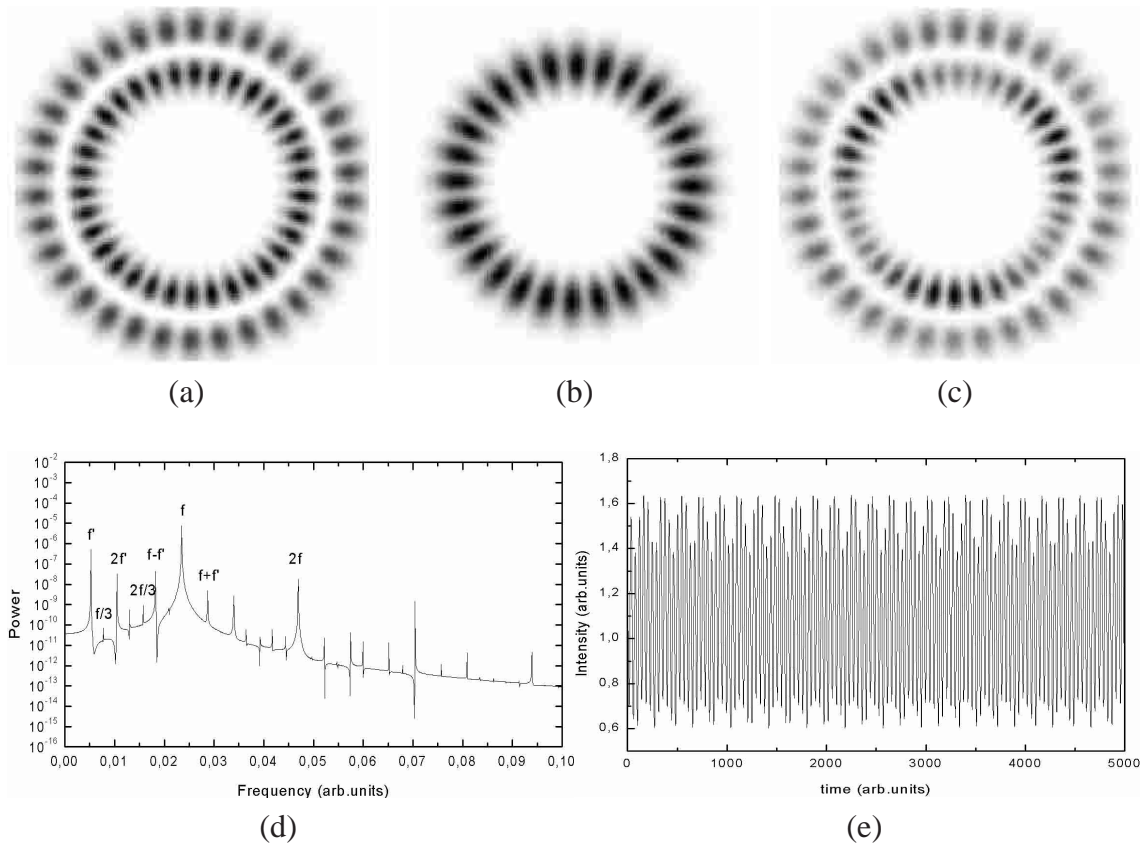


Fig. 6. (a, b) Patterns corresponding to the functions described in equations (12); (c) pattern resulting from the competition of the two functions *via* equations (11); (d) power spectrum of the temporal evolution of the laser intensity; (e) temporal evolution of the laser intensity. The parameters used in equations (11) are $A_1^r = A_2^r = 1.4489$, $A_1^i = 1$, $A_2^i = 4$, $B_1 = 1.05$, $B_2 = 0.15$, $C_1 = C_2 = 0.1$, $\rho_\epsilon = 0.5$, $\varphi_\epsilon = 1.059$.

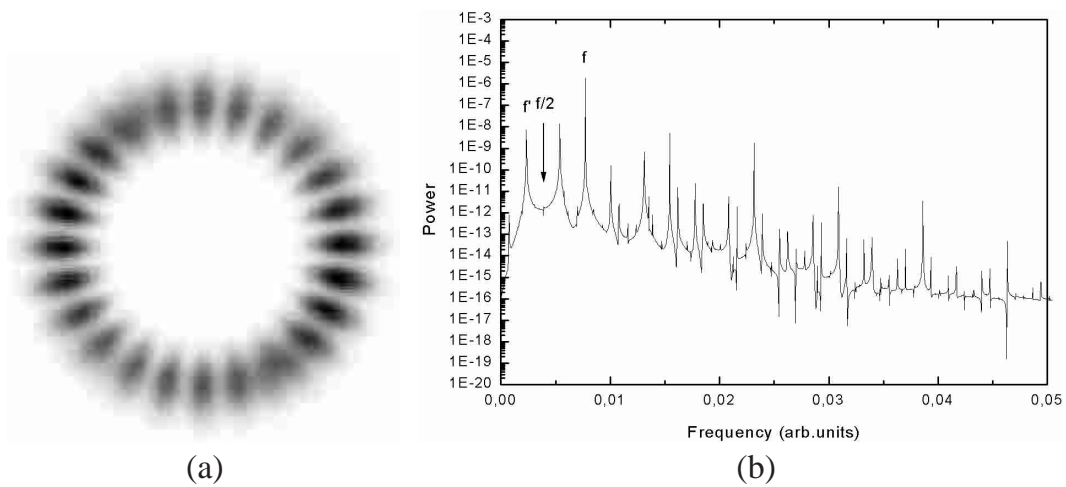


Fig. 7. (a) Pattern resulting from the competition of the two functions described in equations (13) *via* equations (11); (b) power spectrum of the temporal evolution of the laser intensity. The parameters used in equations (11) are $A_1^r = A_2^r = 1.4489$, $A_1^i = 13$, $A_2^i = 12$, $B_1 = 0.5$, $B_2 = 1$, $C_1 = C_2 = 0.1$, $\rho_\epsilon = 0.5$, $\varphi_\epsilon = 1.059$.

4 Conclusions

In this paper we have reported experimental evidence of different dynamical regimes arising from the competition of annular patterns in a CO₂ laser. Chaotic regimes have been observed during the coexistence of different patterns. To reproduce qualitatively the experimentally detected phenomena, we have derived a numerical model from the Maxwell-Bloch equations, including symmetry breaking terms and new cross-mode coupling terms, which enables the interpretation of the main experimental features.

The Authors are indebted with F.T. Arecchi for helpful discussions, and with D.L. Valladares and B. Peña for their valuable help in the elaboration of the simulation program. MLR acknowledges financial support from EU Contract FMRX-CT96-0010, from the Integrated Action HI97-30, and from the *Asociación de Amigos de la Universidad de Navarra*. S.B. acknowledges financial support from EU Contract No. ERBFMBICT983466.

References

1. F. Prati, M. Brambilla, L.A. Lugiato, *Nuovo Cimento* **7**, 1 (1994).
2. D. Dangoisse, D. Hennequin, C. Lepers, E. Louvergneaux, P. Glorieux, *Phys. Rev. A* **46**, 5955 (1992).
3. G. Huyet, M.C. Martinoni, J.R. Tredicce, S. Rica, *Phys. Rev. Lett.* **75**, 4027 (1995).
4. G. Huyet, C. Mathis, J.R. Tredicce, *Opt. Commun.* **127**, 257 (1996).
5. J. Swift, P.C. Hohenberg, *Phys. Rev. A* **15**, 319 (1977).
6. P. Coulet, L. Gil, F. Rocca, *Opt. Commun.* **73**, 403 (1989).
7. Y. Kuramoto, T. Tsuzuki, *Prog. Theor. Phys.* **55**, 356 (1976); G.I. Sivashinsky, *Acta Astron.* **4**, 1177 (1977); Y. Kuramoto, *Chemical Oscillations, Waves and Turbulence* (Springer-Verlag, Berlin, 1984); introduced for lasers in R. Lefever, L.A. Lugiato, W. Kaige, N.B. Abraham, P. Mandel, *Phys. Lett. A* **135**, 254 (1989).
8. H.G. Solari, R. Gilmore, *J. Opt. Soc. Am. B* **7**, 828 (1990).
9. C. Green, G.B. Mindlin, E.J. D'Angelo, H.G. Solari, J.R. Tredicce, *Phys. Rev. Lett.* **65**, 3124 (1990).
10. R. López-Ruiz, G.B. Mindlin, C. Pérez-García, J.R. Tredicce, *Phys. Rev. A* **49**, 4916 (1994).
11. E.J. D'Angelo, E. Izaguirre, G.B. Mindlin, G. Huyet, L. Gil, J.R. Tredicce, *Phys. Rev. Lett.* **68**, 3702 (1992).
12. A. Labate, M. Ciofini, R. Meucci, S. Boccaletti, F.T. Arecchi, *Phys. Rev. A* **56**, 2237 (1997).
13. F.T. Arecchi, G. Giacomelli, P.L. Ramazza, S. Residori, *Phys. Rev. Lett.* **65**, 2531 (1990).
14. M.L. Ramón, R. Meucci, M. Ciofini, A. Labate, L. Calero, *Eur. Phys. J. D* **11**, 137 (2000).
15. P.-Y. Wang, P. Xie, J.-H. Dai, H.-J. Zhang, *Phys. Rev. Lett.* **80**, 4669 (1998).
16. M. Ciofini, A. Labate, R. Meucci, P.-Y. Wang, *Opt. Commun.* **154**, 307 (1998); R. Meucci, A. Labate, M. Ciofini, P.-Y. Wang, *Quant. Semiclass. Opt.* **10**, 803 (1998).
17. G. D'Alessandro, G.L. Oppo, *Opt. Commun.* **88**, 130 (1992).